

High-Pressure Synthesis of $\text{Lu}_2\text{NiIrO}_6$ with Ferrimagnetism and Large Coercivity

Hai L. Feng,[†] Zheng Deng,[‡] Meixia Wu,[§] Mark Croft,^{||} Saul H. Lapidus,[⊥] Sizhan Liu,[#] Trevor A. Tyson,[#] Bruce D. Ravel,[¶] Nicholas F. Quackenbush,[¶] Corey E. Frank,[†] Changqing Jin,[‡] Man-Rong Li,[§] David Walker,[▽] and Martha Greenblatt^{*,†}

[†]Department of Chemistry and Chemical Biology, Rutgers, The State University of New Jersey, 610 Taylor Road, Piscataway, New Jersey 08854, United States

[‡]Institute of Physics, School of Physics, University of Chinese Academy of Sciences, Chinese Academy of Sciences, P. O. Box 603, Beijing 100190, China

[§]Key Laboratory of Bioinorganic and Synthetic Chemistry of Ministry of Education, School of Chemistry, Sun Yat-Sen University, Guangzhou 510275, China

^{||}Department of Physics and Astronomy, Rutgers, The State University of New Jersey, 136 Frelinghuysen Road, Piscataway, New Jersey 08854, United States

[⊥]Advanced Photon Source, Argonne National Laboratory, Lemont, Illinois 60439, United States

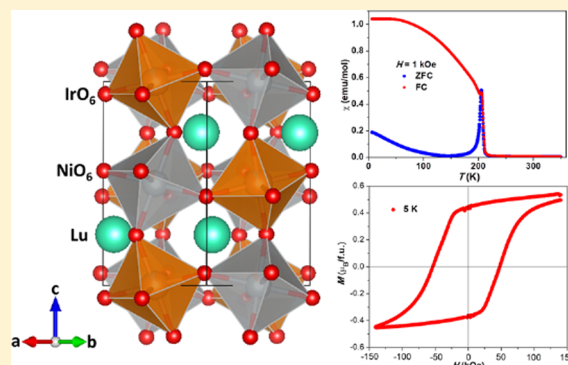
[#]Department of Physics, New Jersey Institute of Technology, Newark, New Jersey 07102, United States

[¶]Materials Measurement Science Division, Material Measurement Laboratory, National Institute of Standards and Technology, Gaithersburg, Maryland 20899, United States

[▽]Lamont Doherty Earth Observatory, Columbia University, 61 Route 9W, PO Box 1000, Palisades, New York 10964, United States

Supporting Information

ABSTRACT: Double-perovskite $\text{Lu}_2\text{NiIrO}_6$ was synthesized at high pressure (6 GPa) and high temperature (1300 °C). Synchrotron powder X-ray diffraction indicates that its structure is a monoclinic double perovskite (space group $P2_1/n$) with a small, 11% Ni/Ir antisite disorder. X-ray absorption near-edge spectroscopy measurements established Ni^{2+} and Ir^{4+} formal oxidation states. Magnetic studies indicate a ferrimagnetic transition at 207 K. The low-temperature magnetization curve of $\text{Lu}_2\text{NiIrO}_6$ features broad hysteresis with a coercive field as high as 48 kOe. These results encourage the search for hard magnets in the class of 3d/5d double-perovskite oxides.



INTRODUCTION

Double-perovskite (DP) oxides have the general formula of $\text{A}_2\text{BB}'\text{O}_6$. DP oxides with 3d and 4d/5d transition-metal (TM) cations at the B and B' sites, respectively, continue to attract attention because of their interesting physical properties including high-temperature ferrimagnetism, half-metallic, ferro- or ferrimagnetic insulation, large magnetoresistance, and exchange bias.^{1–16} The room-temperature magnetoresistance observed in half-metallic $\text{Sr}_2\text{FeMoO}_6$, which has a Curie temperature (T_C) of 415 K, showed prospects for spintronic applications.^{1,2} Recently, reports of 3d/5d DP oxides continue to show much progress in the synthesis of 3d/5d DP oxides with respect to high-temperature magnetic ordering and other novel properties.^{3–16} Relative to 3d, 5d elements generally have larger spin–orbit coupling (SOC) and smaller on-site Coulomb repulsion because of more extended

radial orbitals. Consequently, compounds of 5d elements have much different spin, orbital, and the charge degrees of freedom than those of 3d elements.¹⁷ For examples, a novel Mott insulating state in Sr_2IrO_4 ,¹⁸ a metal–insulator transition in NaOsO_3 ,^{19,20} and a transition to a ferroelectric-like metallic state in LiOsO_3 ²¹ were reported in 5d solid-state oxides.

Many DP oxides containing both 3d and 5d TM ions display interesting properties:^{5–16} $\text{Sr}_2\text{CrReO}_6$ is half-metallic and high-temperature ferrimagnetic (FiM) with $T_C = 635$ K.⁷ Transition-metal-only DPs Mn_2BReO_6 (B = Fe and Mn) display magnetic and magnetoresistive behavior,^{10,11} whereas insulating $\text{Sr}_2\text{CrOsO}_6$ and $\text{Ca}_2\text{FeOsO}_6$ feature above-room-temperature FiM transitions.^{12–14} Typically, DP oxides have

Received: September 7, 2018

Published: December 17, 2018

an ordered rocksalt and three-dimensional arrangement of corner-sharing BO_6 and $\text{B}'\text{O}_6$ octahedra and form interpenetrating B and B' face-centered cubic sublattices. Thus, the magnetic properties are generally determined by exchange interactions between the intra- and inter-sublattices, which are correlated with structural distortions.^{22–29}

As an obvious strategy, substitution of smaller cations into the A-site would be expected to introduce significant structural distortions and affect the magnetic properties by magneto-structural coupling. Thus, magnetodielectric effects were reported in $\text{Sc}_2\text{NiMnO}_6$.³⁰ In $\text{Ln}_2\text{NiIrO}_6$ (Ln = La, Pr, Nd, and Sm–Gd), the structural distortions enhance the FiM ordering temperature, with the highest $T_C = 170$ K for $\text{Gd}_2\text{NiIrO}_6$.^{31–33}

In this work, we aimed to introduce small cations, Lu and Sc, into the A-site of A_2NiIrO_6 by high-pressure and high-temperature synthesis. $\text{Lu}_2\text{NiIrO}_6$ was successfully synthesized under 6 GPa and 1300 °C, but $\text{Sc}_2\text{NiIrO}_6$ could not be prepared with pressure up to 8 GPa and 1300 °C. Magnetic studies reveal $\text{Lu}_2\text{NiIrO}_6$ with a higher FiM transition (207 K) than that of $\text{Gd}_2\text{NiIrO}_6$ (170 K)³¹ and with a large coercivity of 48 kOe at 5 K. These results motivate the search for hard magnetic materials in 3d/5d DP oxides.

EXPERIMENTAL SECTION

Synthesis and Synchrotron Powder X-ray Diffraction.

Polycrystalline samples of $\text{Lu}_2\text{NiIrO}_6$ were synthesized by solid-state reactions from Lu_2O_3 (99.9%, Alfa), NiO (99%, Alfa), and IrO_2 (99.99%, Alfa). A molar ratio 1:1:1 of Lu_2O_3 , NiO, and IrO_2 was well ground and sealed in a Pt capsule inside a MgO crucible. The precursors were then statically compressed at a pressure of 6 GPa in a Walker-type multianvil press³⁴ and were heated at 1300 °C for 1 h, with the pressure maintained at 6 GPa. The sample was then quenched to ambient temperature by stopping heating before the pressure was slowly released.

Small pieces of $\text{Lu}_2\text{NiIrO}_6$ were ground to a fine powder, which was then characterized by synchrotron powder X-ray diffraction (SPXD, $\lambda = 0.41270$ Å) at ambient temperature at the beamline 11-BM of the Advanced Photon Source (APS) of Argonne National Laboratory. Rietveld refinements of the SPXD data were done with the JANA2006 software,³⁵ and the crystal structures were drawn with the VESTA software.³⁶

X-ray Absorption Near-Edge Spectroscopy. The X-ray absorption near-edge spectroscopy (XANES) experiments on $\text{Lu}_2\text{NiIrO}_6$ and standards were performed at the national synchrotron light source (NSLS), NSLS-I and NSLS-II at Brookhaven National Labs. The prior work, on the standards, was performed at NSLS-I on beamlines X19A (X18B) with a Si-111 double-crystal (channel cut) monochromator. The measurement on $\text{Lu}_2\text{NiIrO}_6$ has been carried out at the next-generation NSLS-II facility on the 6-BM, BMM beamline with a Si-311 double-crystal monochromator. The NSLS-II high flux insertion device 8-ID ISS beamline was also used in these measurements. Both transmission mode and fluorescent measurements were made on all samples, and simultaneous standards were used in all measurements for precision energy calibration. Standard linear background and post-edge normalization to unity were used in the analysis.^{37–51}

Transport and Magnetism. Using a polycrystalline pellet, the electrical resistivity (ρ) was measured with direct current (0.1 mA) in a four-point in-line arrangement of a Physical Property Measurement System (PPMS, Quantum Design). Au wires and silver paste were used to make electrical contacts. The temperature dependence of the magnetic susceptibility was measured in the same PPMS. The measurements were conducted under zero-field cooling (ZFC) and field cooling (FC) in the temperature range 2–400 K in an applied magnetic field of 1 kOe. Isothermal magnetization curves were initially recorded for fields up to ± 60 kOe at temperatures of 5, 200,

and 300 K with the same PPMS. As the magnetization curves showed a broad hysteresis and were unsaturated at 5 K, further magnetization curves at 5 K were measured with fields up to ± 140 kOe using another PPMS (PPMS-14T, Quantum Design).

RESULTS AND DISCUSSION

Crystal Structure. The room-temperature SPXD data of $\text{Lu}_2\text{NiIrO}_6$ were successfully refined in a monoclinic DP structure with space group $P2_1/n$ (no. 14); this crystal structure was also adopted by other $\text{Ln}_2\text{NiIrO}_6$ phases.^{31–33} The Rietveld refinements of the SPXD data of $\text{Lu}_2\text{NiIrO}_6$ are shown in Figure 1. In this space group, the Lu and the three O

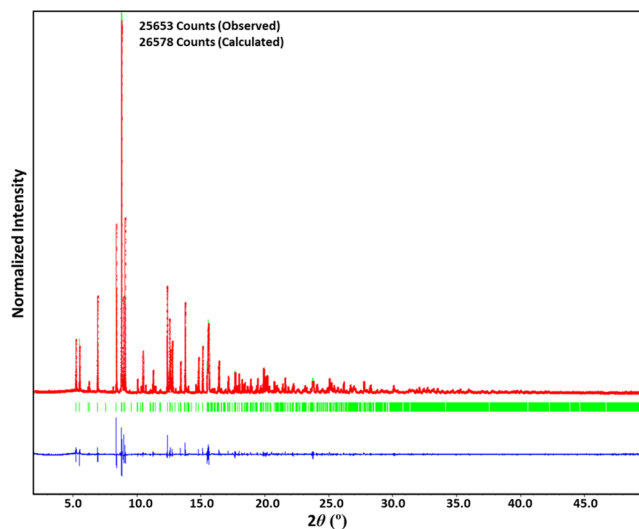


Figure 1. Rietveld analysis of SPXD patterns for $\text{Lu}_2\text{NiIrO}_6$ at room temperature. Red stars and green solid lines show the observed and calculated patterns, respectively. The difference between the observed and calculated patterns is shown as blue lines at the bottom. The green vertical bars indicate positions of expected Bragg reflections for $\text{Lu}_2\text{NiIrO}_6$.

atoms (O1, O2, and O3) fully occupy the Wyckoff positions 4e (x,y,z). The Ni and Ir atoms occupy Wyckoff positions 2b ($1/2,0,0$) and 2c ($1/2,0,1/2$), respectively; however, the refinements revealed a $\sim 11\%$ Ni/Ir antisite disorder. Detailed atomic positions and atomic displacement factors of $\text{Lu}_2\text{NiIrO}_6$ obtained from the SPXD refinements are summarized in Table 1.

The crystal structure of $\text{Lu}_2\text{NiIrO}_6$ based on the SPXD refinement is shown in Figure 2. The corner-sharing Ni- and Ir-dominant octahedra form a rock-salt-like lattice. The inter-octahedral Ni–O–Ir bond angles are $135.4(2)^\circ$, $142.5(3)^\circ$, and $140.8(3)^\circ$, which deviate strongly from 180° and indicate strong octahedral tilting. The bond distances for the local coordination of Ni and Ir ions are summarized in Table 2. These values are comparable to those in other Ni^{2+} and Ir^{4+} DP. Bond valence sum⁵² (BVS), calculated from the bond distances, is 2.33 and 3.77 for the Ni- and Ir-dominant octahedral sites, respectively. The parameters $B = 0.37$, $R_0(\text{Ni}^{2+}) = 1.675$, and $R_0(\text{Ir}^{4+}) = 1.87$ were used for the calculation.⁵³ The somewhat larger BVS for Ni^{2+} -dominant sites and smaller BVS for Ir^{4+} -dominant sites may reflect the effect of antisite disorder between Ni and Ir sites.

X-ray Absorption Near-Edge Spectroscopy. To further examine the valence states of Ni and Ir in $\text{Lu}_2\text{NiIrO}_6$, the Ni-K edges and Ir-L₃ edges of XANES were measured. XANES is

Table 1. Atomic Positions and Atomic Displacement Factors of $\text{Lu}_2\text{NiIrO}_6$ at Ambient Temperature^a

atom	Wyckoff positions	occupancy	x	y	z	U_{iso} (\AA^2)
Lu	4e	1	0.97550(7)	0.07858(5)	0.25076(6)	0.00377(8)
Ir1/Ni1	2c	0.888/0.112(1)	0.5	0	0.5	0.00144(8)
Ni2/Ir2	2b	0.888/0.112(1)	0.5	0	0	0.00144(8)
O1	4e	1	0.1372(8)	0.4484(7)	0.2521(7)	0.0010(6)
O2	4e	1	0.6820(9)	0.3061(9)	0.0592(7)	0.0010(6)
O3	4e	1	0.1786(9)	0.1880(9)	0.9396(7)	0.0010(6)

^aSpace group $P2_1/n$ (no. 14), $a = 5.21431(2)$ \AA , $b = 5.63533(2)$ \AA , $c = 7.53905(2)$ \AA , $\beta = 90.1834(3)^\circ$, $Z = 2$, and $V = 221.529(1)$ \AA^3 . $R_{\text{wp}} = 12.58\%$, $R_p = 9.40\%$, and $\chi^2 = 1.94$.

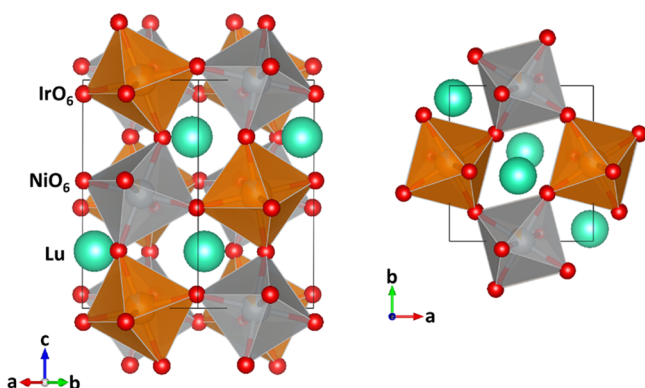


Figure 2. Crystal structures of $\text{Lu}_2\text{NiIrO}_6$, in which IrO_6 and NiO_6 are drawn as octahedra. Lu and O atoms are shown as green and red solid spheres.

Table 2. Selected Bond Distances for $\text{Lu}_2\text{NiIrO}_6$

bond	bond length (\AA)
Ir1/Ni1–O1	$2.049(5) \times 2$
Ir1/Ni1–O2	$2.036(5) \times 2$
Ir1/Ni1–O3	$2.042(5) \times 2$
Ni2/Ir2–O1	$2.025(5) \times 2$
Ni2/Ir2–O2	$2.018(5) \times 2$
Ni2/Ir2–O3	$2.033(5) \times 2$

used for locally probing the valence states of ions in solids. The near-edge characteristics at the K edges of 3d transition-metal, TM(3d), compounds are due to transitions from the 1s to 4p states of the TM, combined with a step feature for the continuum onset.^{37–51} Multiple 4p states associated with different local ligand coordinations, polyhedra edge/corner sharing, mixed 3d configurations (3d–4p), and different orbital orientations complicate near-edge structure.^{38–40,42} Nevertheless, the systematic TM(3d)-K main-edge energy shift to higher energy with increasing oxidation state can serve as a signature of charge transfer in such compounds.^{37–51}

The Ni-K main edge of $\text{Lu}_2\text{NiIrO}_6$ is compared to various standard oxide compound spectra (with octahedral TM–O coordination) in Figure 3. Here, the multiple edge-sharing octahedra in NiO standard and the single perovskite layer in the La_2NiO_4 standard lead to additional splittings in the main-edge p-feature peak.^{41,42} The steep rising edge onset of the $\sim\text{Ni}^{2+}$, $\text{Lu}_2\text{NiIrO}_6$ spectrum coincides well with the $\sim\text{Ni}^{2+}$ standard spectra. The anomalous broadening on the high-energy side of the p-feature peak should be noted. Whether this is due to the high degree of octahedral tilting in the crystal structure, or to an admixture of Ni^{3+} (the Ni on valence sum is 2.33), or due to the Ni–O octahedra distortion into four $2.044(2)$ \AA and two $2.076(2)$ \AA is at present unknown. In the

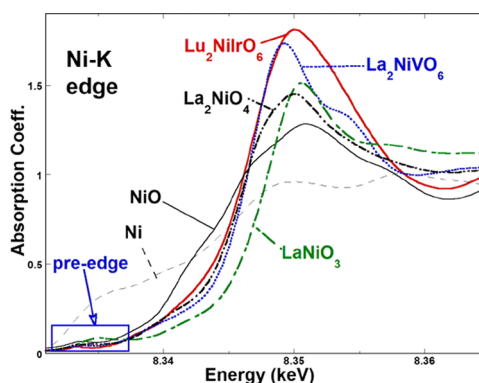


Figure 3. Ni-K edge of $\text{Lu}_2\text{NiIrO}_6$ compared to those of standard compounds: Ni^0 , elemental Ni; $\sim\text{Ni}^{2+}$, NiO, La_2NiVO_6 , La_2NiO_4 ; and $\sim\text{Ni}^{3+}$, LaNiO_3 . Note the pre-edge region, discussed in the Supporting Information, is identified.

Supporting Information, the Ni-K pre-edge feature results (see Figure S1) also support the $\sim\text{Ni}^{2+}$ configuration in this material.

The L_3 edges of 5d TMs are dominated by very intense “white line” (WL) features because of dipole transitions into final d states (see Figures 4 and S2).^{39,43–51} One signature of increasing TM-valence states (decreasing d-count) is the chemical shift of the centrum of the WL-feature to higher

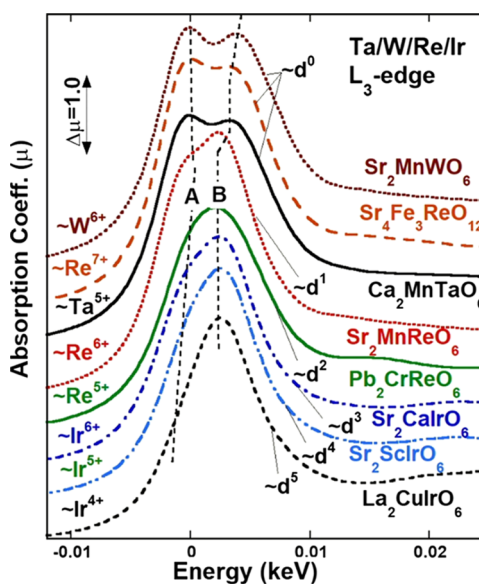


Figure 4. Systematic TM- L_3 edge WL-feature variation with 5d-electron (hole) count from d^0 to d^5 (10–5), note the bimodal A/B structure corresponding to transitions into t_{2g}/e_g final states.

energy.^{43–51} The WL-feature and its chemical shift are illustrated by the prominent shift between $\text{Lu}_2\text{NiIrO}_6$ and $\text{Sr}_2\text{CaIrO}_6$ spectra in Figure S2. The chemical shifts of Ir compounds will be returned to latter after the WL-feature structure is discussed, as discussed in the Supporting Information; the energy of the “continuum resonance” (CR) feature (see Figure S2)^{43,44} is indicative of the Ir–O first-shell bond length and therefore of the Ir-valence. The CR-feature results in the Supporting Information section suggest an $\sim\text{Ir}^{4+}$ configuration.

Perhaps, the strongest signature of increasing 5d-TM-valence states (decreasing d-count) lies in the dramatic, systematic evolution of the prominent bimodal A/B structure of the WL-feature for octahedrally coordinated TM–O compounds, as illustrated in Figure 4.^{40,43–51} This bimodal A (t_{2g} related)/B (e_g related) structure arises from the octahedral O-ligand coordination ligand field (LF), splitting of the d-states, into lower energy, 6X degenerate, t_{2g} and higher energy, 4X degenerate, e_g multiplets.^{40,43–51} This LF splitting is most clearly illustrated in the d^0 compound spectra shown in Figure 4. The systematic filling of the t_{2g} orbitals with increasing 5d-orbital count (decreasing final state hole-count) clearly leads to a systematic decrease of the A-feature (t_{2g} -hole coupled) intensity as is illustrated in Figure 4 for a series of compounds spanning d^0 – d^5 .^{40,43–51} Here, the spectra of the various compounds have been displaced to nominally align the A/B features.

Figure 5 shows a detailed comparison of the Ir- L_3 WL features of $\text{Lu}_2\text{NiIrO}_6$ along with the standard spectra for

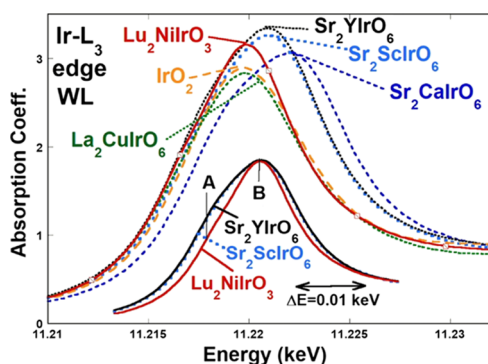


Figure 5. Ir- L_3 WL features of $\text{Lu}_2\text{NiIrO}_6$ along with the standard spectra for $\sim\text{Ir}^{6+}\text{-d}^3$, $\text{Sr}_2\text{CaIrO}_6$; $\sim\text{Ir}^{5+}\text{-d}^4$, $\text{Sr}_2\text{ScIrO}_6$, and Sr_2YIrO_6 ; and $\sim\text{Ir}^{4+}\text{-d}^5$, IrO_2 , and $\text{La}_2\text{CuIrO}_6$. Inset: An expanded superimposed comparison of the $\text{Lu}_2\text{NiIrO}_6$ and $\sim\text{Ir}^{5+}\text{-d}^4$ standard spectra illustrating the decreased A-feature intensity in the former. Note that the $\text{Lu}_2\text{NiIrO}_6$ spectrum is narrower because of higher energy resolution and that the superimposed spectra involve an energy shift and amplitude rescaling.

$\sim\text{Ir}^{6+}\text{-d}^3$, $\text{Sr}_2\text{CaIrO}_6$; $\sim\text{Ir}^{5+}\text{-d}^4$, $\text{Sr}_2\text{ScIrO}_6$, and Sr_2YIrO_6 ; and $\sim\text{Ir}^{4+}\text{-d}^5$, IrO_2 , and $\text{La}_2\text{CuIrO}_6$. The first point to note is the clear systematic chemical shift of the WL feature to lower energy in the $\sim\text{Ir}^{6+}\text{-d}^3$ to $\sim\text{Ir}^{5+}\text{-d}^4$ to $\sim\text{Ir}^{4+}\text{-d}^5$ sequence of spectra. The $\text{Lu}_2\text{NiIrO}_6$ spectrum clearly falls in an energy range consistent with an $\sim\text{Ir}^{4+}\text{-d}^5$ configuration.

The second point to note is the systematic decrease of the A-feature intensity (relative to the B-feature) in the same $\sim\text{Ir}^{6+}\text{-d}^3$ to $\sim\text{Ir}^{5+}\text{-d}^4$ to $\sim\text{Ir}^{4+}\text{-d}^5$ sequence of spectra. The grounding of this effect in the filling of the t_{2g} states (decreasing availability of t_{2g} -final-hole-states) was noted in the discussion of the spectra in Figure 4, where the large A/B

variation between d^0 and d^5 is abundantly clear. In order to clarify this effect for $\text{Lu}_2\text{NiIrO}_6$, its spectrum is displayed on an expanded scale in the inset of Figure 5 superimposed with the $\sim\text{Ir}^{5+}\text{-d}^4$ standards. Here, the standard spectra have been displaced in energy to compensate for the chemical shift and have been modestly rescaled for the sake of superposition. It should also be noted that the $\text{Lu}_2\text{NiIrO}_6$ spectrum is sharper because it was collected with a higher resolution Si-311 monochromator crystal on NSLS-II beamline 6-BM. The decreased A-feature intensity in the $\text{Lu}_2\text{NiIrO}_6$ spectrum (relative to the $\sim\text{Ir}^{5+}\text{-d}^4$ standards) is clear in the inset. Moreover, a small vestigial A-feature intensity remains in the $\text{Lu}_2\text{NiIrO}_6$ spectrum consistent with its approximately one remaining t_{2g} hole state. Thus, the WL-A/B feature intensities, the WL-feature chemical shift, and the CR fine structure feature all combine to support an $\sim\text{Ir}^{4+}\text{-d}^5$ configuration for $\text{Lu}_2\text{NiIrO}_6$.

Transport. The temperature dependence of electrical resistivity of a polycrystalline sample of $\text{Lu}_2\text{NiIrO}_6$ is shown in Figure 6. $\text{Lu}_2\text{NiIrO}_6$ displays semiconducting behavior as its

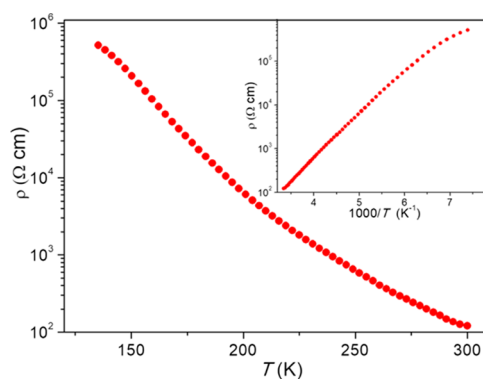


Figure 6. Temperature dependence of the electrical resistivity of $\text{Lu}_2\text{NiIrO}_6$. The inset shows the corresponding plots with T^{-1} scale.

resistivity increases by several orders of magnitude when the temperature decreases from 300 K to lower temperatures. The resistivity exceeds the measurement limit when temperatures are lower than 135 K. The data are roughly linear on a T^{-1} scale as shown in the inset of Figure 6, which is in accordance with an activated transport model. An estimated activation energy E_a of 0.39 eV was obtained by fitting the Arrhenius equation to these data.

Magnetism. The temperature dependence of the magnetic susceptibility, χ , of $\text{Lu}_2\text{NiIrO}_6$ in Figure 7 shows a sharp increase of χ below ~ 207 K indicative of a possible ferromagnetic (FM) or FiM transition. The ZFC and FC data start to deviate below the transition temperature; similar phenomena were observed in analogous DPs $\text{Ln}_2\text{NiIrO}_6$ ($\text{Ln} = \text{La}, \text{Pr}, \text{Nd}, \text{and Sm-Gd}$)³¹ and $\text{Ca}_2\text{NiOsO}_6$.⁵⁴ An attempt to fit the 350–400 K data with the Curie–Weiss (CW) law (as shown in the inset of Figure 7) resulted in a CW temperature (θ_{CW}) of -37 K and an effective magnetic moment (μ_{eff}) per formula unit (f.u.) of $3.47 \mu_B$. The negative θ_{CW} indicates that in $\text{Lu}_2\text{NiIrO}_6$, anti-FM (AFM) interactions are dominant and that the magnetically ordered state is likely FiM. The experimentally obtained μ_{eff} of $3.47 \mu_B$ is consistent with the calculated spin-only $\mu_{\text{eff}} = 3.32 \mu_B/\text{f.u.}$ and comparable to μ_{eff} of $3.28 \mu_B$ reported for the isoelectronic $\text{La}_2\text{NiIrO}_6$.³¹ However, the real nature of the magnetic state of Ir^{4+} remains

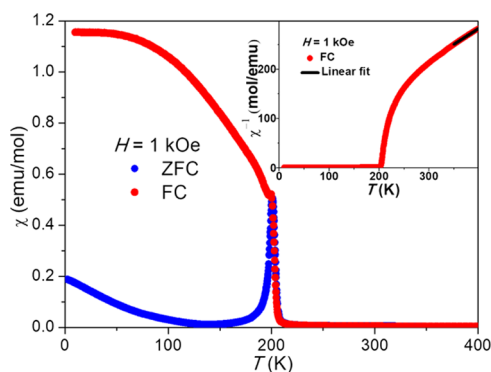


Figure 7. Temperature dependence of the magnetic susceptibility of $\text{Lu}_2\text{NiIrO}_6$ measured at $H = 1$ kOe. The inset shows the reciprocal χ versus temperature.

questionable because in an octahedral crystal field, the orbital angular momentum of the three t_{2g} orbitals may entangle with the spin moments and form an upper $j_{\text{eff}} = 1/2$ doublet and a lower $j_{\text{eff}} = 3/2$ quadruplet when strong SOC is present. The well-studied Mott insulating state in Sr_2IrO_4 (Ir^{4+} and t_{2g}^5) is understood with this scenario.¹⁸

To further understand the magnetic transition, isothermal magnetization curves, $M(H)$, of $\text{Lu}_2\text{NiIrO}_6$ were measured at temperatures above and below the ordering temperature (Figure 8). At 300 K, the linear behavior of the $M(H)$ data indicates a paramagnetic state. The $M(H)$ plot recorded at 200 K is supportive of an FM or FiM state. The $M(H)$ data at 5 K between -140 and $+140$ kOe, as shown in Figure 8b, show that the hysteresis loop is not closed. The magnetization is not saturated and is about $0.52 \mu_{\text{B}}/\text{f.u.}$. The observed magnetization

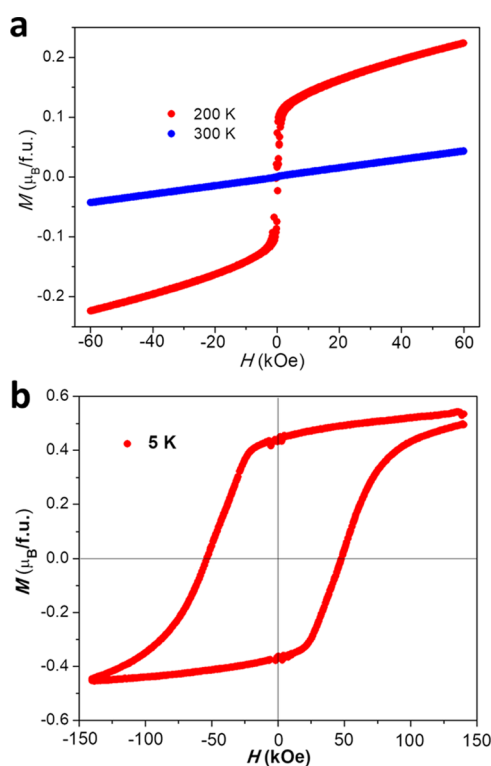


Figure 8. (a) Isothermal magnetization of $\text{Lu}_2\text{NiIrO}_6$ measured at 200 and 300 K and (b) isothermal magnetization of $\text{Lu}_2\text{NiIrO}_6$ measured at 5 K.

($0.52 \mu_{\text{B}}/\text{f.u.}$) is much lower than the theoretically calculated spin-only moment of $3.0 \mu_{\text{B}}/\text{f.u.}$, assuming that Ni^{2+} has $t_{2g}^6 e_g^2 S = 1$ and Ir^{4+} has $t_{2g}^5 S = 1/2$ electronic configuration and that they are ferromagnetically coupled. Nevertheless, it is close to the difference of Ni^{2+} and Ir^{4+} spin-only moment ($1.0 \mu_{\text{B}}/\text{f.u.}$). The data, therefore, indicate a FiM order. The specific heat in Figure 9 shows a lambda-type feature at 207 K, which confirms

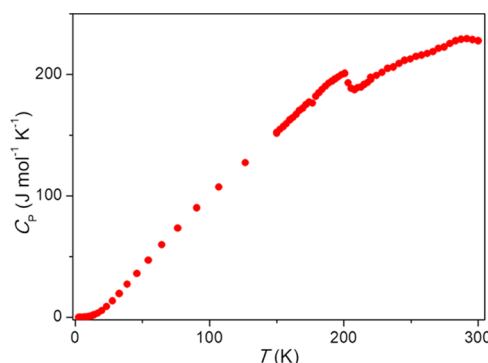


Figure 9. Temperature dependence of the specific heat of $\text{Lu}_2\text{NiIrO}_6$.

the long-range magnetic order in $\text{Lu}_2\text{NiIrO}_6$. In Figure 8, the $M(H)$ data of $\text{Lu}_2\text{NiIrO}_6$ at 5 K display a remarkably high coercive field $H_C = 48$ kOe, which is much larger than the $H_C \approx 14$ kOe observed in $\text{Eu}_2\text{NiIrO}_6$.³¹

The disagreement between the experimental ($0.52 \mu_{\text{B}}/\text{f.u.}$) and theoretical FiM spin-only moment ($1.0 \mu_{\text{B}}/\text{f.u.}$) magnetization is attributed to the unsaturated $M(H)$ curve and antisite disorder of Ni/Ir atoms of $\text{Lu}_2\text{NiIrO}_6$. The antisite disorder is known to decrease the magnetic moment by $M = M_{\text{exp}} \times (1 - 2AS)$. M_{exp} is the theoretical spin-only moment, and AS is the degree of antisite disorder.^{55–58} In $\text{Lu}_2\text{NiIrO}_6$, M_{exp} is $1 \mu_{\text{B}}/\text{f.u.}$ and AS is 0.11 (11% disorder). When the effect of antisite disorder was considered, the theoretical spin-only moment for $\text{Lu}_2\text{NiIrO}_6$ was $0.78 \mu_{\text{B}}/\text{f.u.}$ which is approaching the observed moment of $0.52 \mu_{\text{B}}/\text{f.u.}$. It should be noted that the spin-only scenario is unlikely to be valid because of the strong SOC of Ir ions.¹⁸ Theoretical studies of ferrimagnetic $\text{La}_2\text{CoIrO}_6$ and $\text{La}_2\text{NiIrO}_6$ indicate that the orbital contribution ($m_L = 0.43 \mu_{\text{B}}/\text{Ir}$ for $\text{La}_2\text{CoIrO}_6$ and $0.32 \mu_{\text{B}}/\text{Ir}$ for $\text{La}_2\text{NiIrO}_6$) of Ir^{4+} is comparable with the spin contribution ($m_S = 0.44 \mu_{\text{B}}/\text{Ir}$ for $\text{La}_2\text{CoIrO}_6$ and $0.32 \mu_{\text{B}}/\text{Ir}$ for $\text{La}_2\text{NiIrO}_6$).^{59,60} However, an X-ray magnetic circular dichroism (XMCD) study of $\text{La}_2\text{CoIrO}_6$ derived an $m_S = 0.205 \mu_{\text{B}}/\text{Ir}$ and an $m_L = 0.177 \mu_{\text{B}}/\text{Ir}$.⁶¹ A future XMCD study on $\text{Lu}_2\text{NiIrO}_6$ could further clarify this issue.

$\text{Lu}_2\text{NiIrO}_6$, compared with $\text{Ln}_2\text{NiIrO}_6$ ($\text{Ln} = \text{La}, \text{Pr}, \text{Nd}$, and $\text{Sm}-\text{Gd}$),^{31–33} shows the smallest Ni–O–Ir bond angle (see Figure 10), or the largest structural distortions, and the highest ordering temperature. The structure–property relationship for Ni–Ir-based DPs is clearly revealed in Figure 10: the greater the structural distortions, the higher the magnetic ordering temperature. A similar correlation was also observed in the 3d/5d DPs $\text{Ca}_{2-x}\text{Sr}_x\text{FeOsO}_6$.^{22,27} The ferrimagnetic nature of $\text{Lu}_2\text{NiIrO}_6$ indicates that Ni^{2+} and Ir^{4+} ions are AFM coupled, indicating that the AFM $\text{Ni}^{2+}-\text{O}-\text{Ir}^{4+}$ interactions are dominant. Because the t_{2g} orbitals of Ni^{2+} are completely filled, the AFM exchange coupling between Ni^{2+} and Ir^{4+} can only be mediated via virtual hopping between half-filled $\text{Ni}-e_g$ and partially filled $\text{Ir}-t_{2g}$ orbitals. However, in the cubic DP structure, where the $\text{Ni}^{2+}-\text{O}-\text{Ir}^{4+}$ pathway is linear, the $\text{Ni}-e_g$

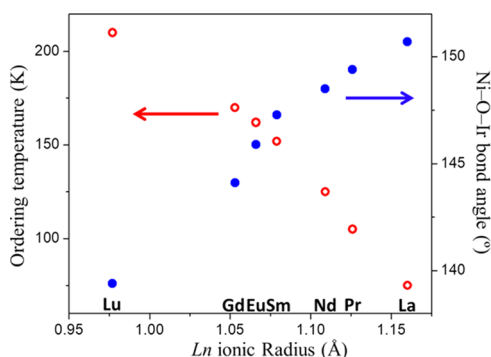


Figure 10. Magnetic ordering temperatures and Ni–O–Ir bond angles of the $\text{Ln}_2\text{NiIrO}_6$ ($\text{Ln} = \text{La}, \text{Pr}, \text{Nd}, \text{Sm}, \text{Eu}, \text{Gd}$, and Lu).

and $\text{Ir-}t_{2g}$ orbitals are orthogonal. Nevertheless, hopping between $\text{Ni-}e_g$ and $\text{Ir-}t_{2g}$ orbitals becomes possible in the distorted DP where the $\text{Ni}^{2+}\text{-O-Ir}^{4+}$ bond angles strongly deviate from 180° .⁶² With increasing structural distortion (relative to other larger Ln A-cations), the AFM exchange coupling between half-filled $\text{Ni-}e_g$ and partially-filled $\text{Ir-}t_{2g}$ orbitals is expected to enhance in $\text{Lu}_2\text{NiIrO}_6$; thus, the magnetic ordering temperatures increase (Figure 10).

CONCLUSIONS

Targeting the preparation of A_2NiIrO_6 DPs with small A-site ions, $\text{Lu}_2\text{NiIrO}_6$ was synthesized at high pressure and temperature. Structural studies with SPXD show that $\text{Lu}_2\text{NiIrO}_6$ adopts a monoclinic DP structure (space group $P2_1/n$) with near Ni/Ir rocksalt-like order. The magnetic data indicate a ferrimagnetic transition below 207 K, which is the highest ordering temperature in Ir-based DP oxides so far. A remarkable feature of the polycrystalline sample of $\text{Lu}_2\text{NiIrO}_6$ is a high coercive field of 48 kOe. These 3d/5d DPs are of interest for hard magnets. High coercivities of 41, 90, and 120 kOe were reported for TM oxides of ferrimagnetic $\text{La}_2\text{Ni}_{1.19}\text{Os}_{0.81}\text{O}_6$, LuFe_2O_4 , and weakly FM $\text{Sr}_3\text{Ru}_{5-x}\text{O}_{15}$, respectively.^{63–65} However, the origin of the observed huge coercivity is not fully understood. Large magnetocrystalline anisotropy, as well as frustration and/or defects (disorder), was found to favor large coercivities.⁶⁴ Because $\text{Lu}_2\text{NiIrO}_6$ has a low-symmetry crystal structure and heavy Ir atoms, a large magnetocrystalline anisotropy is expected.

ASSOCIATED CONTENT

Supporting Information

The Supporting Information is available free of charge on the ACS Publications website at DOI: 10.1021/acs.inorgchem.8b02557.

Discussions about Ni-K pre-edge and CR features of Ir-L3 edge (PDF)

Accession Codes

CCDC 1866087 contains the supplementary crystallographic data for this paper. These data can be obtained free of charge via www.ccdc.cam.ac.uk/data_request/cif, or by emailing data_request@ccdc.cam.ac.uk, or by contacting The Cambridge Crystallographic Data Centre, 12 Union Road, Cambridge CB2 1EZ, UK; fax: +44 1223 336033.

AUTHOR INFORMATION

Corresponding Author

*E-mail: greenbla@chem.rutgers.edu.

ORCID

Trevor A. Tyson: 0000-0001-6587-9296

Man-Rong Li: 0000-0001-8424-9134

Martha Greenblatt: 0000-0002-1806-2766

Notes

The authors declare no competing financial interest.

ACKNOWLEDGMENTS

The work of H.L.F. and M.G. was supported by NSF-DMR 1507252 grant. The works at IOPCAS are supported by NSF & MOST of China through research projects. Part of the work was done at the NSLS II, a U.S. Department of Energy (DOE) Office of Science User Facility operated for the DOE Office of Science by Brookhaven National Laboratory under contract no. DE-SC0012704. The authors wish to thank the NSLS-II scientists Klaus Attenkofer and Eli Stavitski for valuable help in the NSLS-II work. Use of the Advanced Photon Source at Argonne National Laboratory was supported by the U. S. Department of Energy, Office of Science, Office of Basic Energy Sciences, under contract no. DE-AC02-06CH11357.

REFERENCES

- (1) Kobayashi, K.-I.; Kimura, T.; Sawada, H.; Terakura, K.; Tokura, Y. Room-temperature magnetoresistance in an oxide material with an ordered double-perovskite structure. *Nature* **1998**, *395*, 677–680.
- (2) Tomioka, Y.; Okuda, T.; Okimoto, Y.; Kumai, R.; Kobayashi, K.-I.; Tokura, Y. Magnetic and electronic properties of a single crystal of ordered double perovskite $\text{Sr}_2\text{FeMoO}_6$. *Phys. Rev. B: Condens. Matter Mater. Phys.* **2000**, *61*, 422–427.
- (3) Philipp, J. B.; Majewski, P.; Alff, L.; Erb, A.; Gross, R.; Graf, T.; Brandt, M. S.; Simon, J.; Walther, T.; Mader, W.; Topwal, D.; Sarma, D. D. Structural and doping effects in the half-metallic double perovskite A_2CrWO_6 ($\text{A} = \text{Sr}, \text{Ba}, \text{and Ca}$). *Phys. Rev. B: Condens. Matter Mater. Phys.* **2003**, *68*, 144431.
- (4) Maignan, A.; Raveau, B.; Martin, C.; Hervieu, M. Large intragrain magnetoresistance above room temperature in the double perovskite $\text{Ba}_2\text{FeMoO}_6$. *J. Solid State Chem.* **1999**, *144*, 224–227.
- (5) Aréval-López, A. M.; McNally, G. M.; Atfield, J. P. Large magnetization and frustration switching of magnetoresistance in the double-perovskite ferrimagnet $\text{Mn}_2\text{FeReO}_6$. *Angew. Chem., Int. Ed.* **2015**, *54*, 12074–12077.
- (6) Kobayashi, K.-I.; Kimura, T.; Tomioka, Y.; Sawada, H.; Terakura, K.; Tokura, Y. Intergrain tunneling magnetoresistance in polycrystals of the ordered double perovskite $\text{Sr}_2\text{FeReO}_6$. *Phys. Rev. B: Condens. Matter Mater. Phys.* **1999**, *59*, 11159–11162.
- (7) Kato, H.; Okuda, T.; Okimoto, Y.; Tomioka, Y.; Takenoya, Y.; Ohkubo, A.; Kawasaki, M.; Tokura, Y. Metallic ordered double-perovskite $\text{Sr}_2\text{CrReO}_6$ with maximal Curie temperature of 635 K. *Appl. Phys. Lett.* **2002**, *81*, 328–330.
- (8) Kim, T. H.; Uehara, M.; Cheong, S.-W.; Lee, S. Large room-temperature intergrain magnetoresistance in double perovskite $\text{SrFe}_{1-x}(\text{Mo or Re})_x\text{O}_6$. *Appl. Phys. Lett.* **1999**, *74*, 1737–1739.
- (9) Retuerto, M.; Li, M.-R.; Stephens, P. W.; Sánchez-Benítez, J.; Deng, X.; Kotliar, G.; Croft, M. C.; Ignatov, A.; Walker, D.; Greenblatt, M. Half-metallicity in $\text{Pb}_2\text{CoReO}_6$ double perovskite and high magnetic ordering temperature in $\text{Pb}_2\text{CrReO}_6$ perovskite. *Chem. Mater.* **2015**, *27*, 4450–4458.
- (10) Li, M.-R.; Retuerto, M.; Deng, Z.; Stephens, P. W.; Croft, M.; Huang, Q.; Wu, H.; Deng, X.; Kotliar, G.; Sánchez-Benítez, J.; Hadermann, J.; Walker, D.; Greenblatt, M. Giant magnetoresistance in the half-metallic double-perovskite ferrimagnet $\text{Mn}_2\text{FeReO}_6$. *Angew. Chem., Int. Ed.* **2015**, *54*, 12069–12073.

- (11) Li, M.-R.; Hodges, J. P.; Retuerto, M.; Deng, Z.; Stephens, P. W.; Croft, M. C.; Deng, X.; Kotliar, G.; Sánchez-Benítez, J.; Walker, D.; Greenblatt, M. Mn₂MnReO₆: synthesis and magnetic structure determination of a new transition-metal-only double perovskite canted antiferromagnet. *Chem. Mater.* **2016**, *28*, 3148–3158.
- (12) Krockenberger, Y.; Mogare, K.; Reehuis, M.; Tovar, M.; Jansen, M.; Vaitheeswaran, G.; Kanchana, V.; Bultmark, F.; Delin, A.; Wilhelm, F.; Rogalev, A.; Winkler, A.; Alff, L. Sr₂CrOsO₆: End point of a spin-polarized metal-insulator transition by 5d band filling. *Phys. Rev. B: Condens. Matter Mater. Phys.* **2007**, *75*, 020404.
- (13) Samanta, K.; Sanyal, P.; Saha-Dasgupta, T. Half-metallic behavior in doped Sr₂CrOsO₆ double perovskite with high transition temperature. *Sci. Rep.* **2015**, *5*, 15010.
- (14) Feng, H. L.; Arai, M.; Matsushita, Y.; Tsujimoto, Y.; Guo, Y.; Sathish, C. I.; Wang, X.; Yuan, Y.-H.; Tanaka, M.; Yamaura, K. High-temperature ferrimagnetism driven by lattice distortion in double perovskite Ca₂FeOsO₆. *J. Am. Chem. Soc.* **2014**, *136*, 3326–3329.
- (15) Feng, H. L.; Calder, S.; Ghimire, M. P.; Yuan, Y.-H.; Shirako, Y.; Tsujimoto, Y.; Matsushita, Y.; Hu, Z.; Kuo, C.-Y.; Tjeng, L. H.; Pi, T.-W.; Soo, Y.-L.; He, J.; Tanaka, M.; Katsuya, Y.; Richter, M.; Yamaura, K. Ba₂NiOsO₆: a Dirac-Mott insulator with ferromagnetism near 100 K. *Phys. Rev. B: Condens. Matter Mater. Phys.* **2016**, *94*, 235158.
- (16) Feng, H. L.; Adler, P.; Reehuis, M.; Schnelle, W.; Pattison, P.; Hoser, A.; Felser, C.; Jansen, M. High-temperature ferrimagnetism with large coercivity and exchange bias in the partially ordered 3d/5d hexagonal perovskite Ba₂Fe_{1.12}Os_{0.88}O₆. *Chem. Mater.* **2017**, *29*, 886–895.
- (17) Witzak-Krempa, W.; Chen, G.; Kim, Y. B.; Balents, L. Correlated quantum phenomena in the strong spin-orbit regime. *Annu. Rev. Condens. Matter Phys.* **2014**, *5*, 57–82.
- (18) Kim, B. J.; Jin, H.; Moon, S. J.; Kim, J.-Y.; Park, B.-G.; Leem, C. S.; Yu, J.; Noh, T. W.; Kim, C.; Oh, S.-J.; Park, J.-H.; Durairaj, V.; Cao, G.; Rotenberg, E. Novel J_{eff} = 1/2 Mott State Induced by Relativistic Spin-Orbit Coupling in Sr₂IrO₄. *Phys. Rev. Lett.* **2008**, *101*, 076402.
- (19) Shi, Y. G.; Guo, Y. F.; Yu, S.; Arai, M.; Belik, A. A.; Sato, A.; Yamaura, K.; Takayama-Muromachi, E.; Tian, H. F.; Yang, H. X.; Li, J. Q.; Varga, T.; Mitchell, J. F.; Okamoto, S. Continuous metal-insulator transition of the antiferromagnetic perovskite NaOsO₃. *Phys. Rev. B: Condens. Matter Mater. Phys.* **2009**, *80*, No. 161104(R).
- (20) Calder, S.; Garlea, V. O.; McMorro, D. F.; Lumsden, M. D.; Stone, M. B.; Lang, J. C.; Kim, J.-W.; Schlueter, J. A.; Shi, Y. G.; Yamaura, K.; Sun, Y. S.; Tsujimoto, Y.; Christianson, A. D. Magnetically driven metal-insulator transition in NaOsO₃. *Phys. Rev. Lett.* **2012**, *108*, 257209.
- (21) Shi, Y.; Guo, Y.; Wang, X.; Princep, A. J.; Khalyavin, D.; Manuel, P.; Michiue, Y.; Sato, A.; Tsuda, K.; Yu, S.; Arai, M.; Shirako, Y.; Akaogi, M.; Wang, N.; Yamaura, K.; Boothroyd, A. T. A ferroelectric-like structural transition in a metal. *Nat. Mater.* **2013**, *12*, 1024–1027.
- (22) Morrow, R.; Freeland, J. W.; Woodward, P. M. Probing the links between structure and magnetism in Sr_{2-x}Ca_xFeOsO₆ double perovskites. *Inorg. Chem.* **2014**, *53*, 7983–7992.
- (23) Morrow, R.; Soliz, J. R.; Hauser, A. J.; Gallagher, J. C.; Susner, M. A.; Sumption, M. D.; Aczel, A. A.; Yan, J.; Yang, F.; Woodward, P. M. The effect of chemical pressure on the structure and properties of A₂CrOsO₆ (A = Sr, Ca) ferrimagnetic double perovskite. *J. Solid State Chem.* **2016**, *238*, 46–52.
- (24) Morrow, R.; Yan, J.; McGuire, M. A.; Freeland, J. W.; Haskel, D.; Woodward, P. M. Effects of chemical pressure on the magnetic ground states of the osmate double perovskites SrCaCoOsO₆ and Ca₂CoOsO₆. *Phys. Rev. B: Condens. Matter Mater. Phys.* **2015**, *92*, 094435.
- (25) Yuan, Y.; Feng, H. L.; Ghimire, M. P.; Matsushita, Y.; Tsujimoto, Y.; He, J.; Tanaka, M.; Katsuya, Y.; Yamaura, K. High-pressure synthesis, crystal structures, and magnetic properties of 5d double-perovskite oxides Ca₂MgOsO₆ and Sr₂MgOsO₆. *Inorg. Chem.* **2015**, *54*, 3422–3431.
- (26) Wang, H.; Zhu, S.; Ou, X.; Wu, H. Ferrimagnetism in the double perovskite Ca₂FeOsO₆: A density functional study. *Phys. Rev. B: Condens. Matter Mater. Phys.* **2014**, *90*, 054406.
- (27) Hou, Y. S.; Xiang, H. J.; Gong, X. G. Lattice-distortion induced magnetic transition from low-temperature antiferromagnetism to high-temperature ferrimagnetism in double perovskites A₂FeOsO₆ (A=Ca, Sr). *Sci. Rep.* **2015**, *5*, 13159.
- (28) Feng, H. L.; Yamaura, K.; Tjeng, L. H.; Jansen, M. The role of nonmagnetic d⁰ vs. d¹⁰ B-type cations on the magnetic exchange interactions in osmium double perovskites. *J. Solid State Chem.* **2016**, *243*, 119–123.
- (29) Yi, W.; Liang, Q.; Matsushita, Y.; Tanaka, M.; Belik, A. A. High-pressure synthesis, crystal structure, and properties of In₂NiMnO₆ with antiferromagnetic order and field-induced phase transition. *Inorg. Chem.* **2013**, *52*, 14108–14115.
- (30) Yi, W.; Princep, A. J.; Guo, Y.; Johnson, R. D.; Khalyavin, D.; Manuel, P.; Senyshyn, A.; Presniakov, I. A.; Sobolev, A. V.; Matsushita, Y.; Tanaka, M.; Belik, A. A.; Boothroyd, A. T. Sc₂NiMnO₆: a double-perovskite with a magnetodielectric response driven by multiple magnetic orders. *Inorg. Chem.* **2015**, *54*, 8012–8021.
- (31) Ferreira, T.; Morrison, G.; Yeon, J.; zur Loye, H.-C. Design and crystal growth of magnetic double perovskite double perovskite iridates: Ln₂MIrO₆ (Ln = La, Pr, Nd, Sm-Gd; M = Mg, Ni). *Cryst. Growth Des.* **2016**, *16*, 2795–2803.
- (32) Powell, A. V.; Gore, J. G.; Battle, P. D. The magnetic properties of iridium in mixed-metal oxides. *J. Alloys Compd.* **1993**, *201*, 73–84.
- (33) Currie, R. C.; Vente, J. F.; Frikkee, E.; Ijdo, D. J. W. The structure and magnetic properties of La₂MIrO₆ with M = Mg, Co, Ni, and Zn. *J. Solid State Chem.* **1995**, *116*, 199–204.
- (34) Walker, D.; Carpenter, M. A.; Hitch, C. M. Some simplifications to multianvil devices for high pressure experiments. *Am. Mineral.* **1990**, *75*, 1020–1028.
- (35) Petříček, V.; Dušek, M.; Palatinus, L. Crystallographic computing system JANA2006: General features. *Z. Kristallogr.—Cryst. Mater.* **2014**, *229*, 345–352.
- (36) Momma, K.; Izumi, F. VESTA: a three-dimensional visualization system for electronic and structural analysis. *J. Appl. Crystallogr.* **2008**, *41*, 653–658.
- (37) Croft, M.; Sills, D.; Greenblatt, M.; Lee, C.; Cheong, S.-W.; Ramanujachary, K. V.; Tran, D. Systematic Mn-d configuration change in the La_{1-x}Ca_xMnO₃ system: a Mn-K edge XAS study. *Phys. Rev. B: Condens. Matter Mater. Phys.* **1997**, *55*, 8726–8732.
- (38) Sahiner, A.; Croft, M.; Guha, S.; Perez, I.; Zhang, Z.; Greenblatt, M.; Metcalf, P. A.; Jahns, H.; Liang, G. Polarized XAS studies of ternary nickel oxides. *Phys. Rev. B: Condens. Matter Mater. Phys.* **1995**, *51*, 5879–5886.
- (39) Sahiner, A.; Croft, M.; Zhang, Z.; Greenblatt, M.; Perez, I.; Metcalf, P.; Jhans, H.; Liang, G.; Jeon, Y. Electronic structure anisotropy and d-configuration in Ni-based materials. *Phys. Rev. B: Condens. Matter Mater. Phys.* **1996**, *53*, 9745–9752.
- (40) Huang, Y.-H.; Liang, G.; Croft, M.; Lehtimäki, M.; Karppinen, M.; Goodenough, J. B. Double perovskite anode materials Sr₂MMoO₆ (M = Co, Ni) for solid-oxide fuel cells. *Chem. Mater.* **2009**, *21*, 2319–2326.
- (41) Mandal, T. K.; Croft, M.; Hadermann, J.; Van Tendeloo, G.; Stephens, P. W.; Greenblatt, M. La₂MnVO₆ double perovskite: a structural, magnetic and x-ray absorption investigation. *J. Mater. Chem.* **2009**, *19*, 4382–4390.
- (42) Li, M.-R.; Retuerto, M.; Go, Y. B.; Emge, T. J.; Croft, M.; Ignatov, A.; Ramanujachary, K. V.; Dachraoui, W.; Hadermann, J.; Tang, M.-B.; Zhao, J.-T.; Greenblatt, M. Synthesis, crystal structure, and properties of KSB₃O₃-type Bi₃Mn_{1.9}Te_{1.1}O₁₁. *J. Solid State Chem.* **2013**, *197*, 543–549.
- (43) Popov, G.; Greenblatt, M.; Croft, M. Large effects of a-site average cation size on the properties of the double perovskites Ba_{2-x}Sr_xMnReO₆, a d⁵-d¹ system. *Phys. Rev. B: Condens. Matter Mater. Phys.* **2003**, *67*, 024406.

- (44) Lin, Q.; Greenblatt, M.; Croft, M. Evolution of structure and magnetic properties in electron-doped double perovskites, $\text{Sr}_{2-x}\text{La}_x\text{MnWO}_6$ ($0 \leq x \leq 1$). *J. Solid State Chem.* **2005**, *178*, 1356–1366.
- (45) Whaley, L.; Lobanov, M. V.; Sheptyakov, D.; Croft, M.; Ramanujachary, K. V.; Lofland, S.; Stephens, P. W.; Her, J.-H.; Van Tendeloo, G.; Rossell, M.; Greenblatt, M. $\text{Sr}_3\text{Fe}_{3/4}\text{Mo}_{3/4}\text{O}_{6.9}$, an $n = 2$ ruddlesden-popper phase: synthesis and properties. *Chem. Mater.* **2007**, *18*, 3448–3457.
- (46) Mandal, T. K.; Poltavets, V. V.; Croft, M.; Greenblatt, M. structure and magnetic properties of $\text{A}_2\text{MnB}'\text{O}_6$ ($\text{A} = \text{Ca}, \text{Sr}$; $\text{B}' = \text{Sb}, \text{Ta}$) double perovskites. *J. Solid State Chem.* **2008**, *181*, 2325–2331.
- (47) Retuerto, M.; Li, M.-R.; Go, Y. B.; Ignatov, A.; Croft, M.; Ramanujachary, K. V.; Herber, R. H.; Nowik, I.; Hodges, J. P.; Dachraoui, W.; Hadermann, J.; Greenblatt, M. High magnetic ordering temperature in the perovskites ($x = 0.0, 1.0, 2.0$). *J. Solid State Chem.* **2012**, *194*, 48–58.
- (48) Li, M.-R.; Walker, D.; Retuerto, M.; Sarkar, T.; Hadermann, J.; Stephens, P. W.; Croft, M.; Ignatov, A.; Grams, C. P.; Hemberger, J.; Nowik, I.; Halasyamani, P. S.; Tran, T. T.; Mukherjee, S.; Dasgupta, T. S.; Greenblatt, M. Mn_2FeMO_6 ($\text{M} = \text{Nb}, \text{Ta}$)-polar oxides with LiNbO_3 -type structure: high pressure synthesis. *Angew. Chem., Int. Ed.* **2013**, *52*, 8406–8410.
- (49) Kayser, P.; Martínez-Lope, M. J.; Alonso, J. A.; Retuerto, M.; Croft, M.; Ignatov, A.; Fernández-Díaz, M. T. Crystal structure, phase transitions and magnetic properties of iridium (VI) perovskites Sr_2MIR_6 ($\text{M} = \text{Ni}, \text{Zn}$). *Inorg. Chem.* **2013**, *52*, 11013–11022.
- (50) Kayser, P.; Martínez-Lope, M. J.; Alonso, J. A.; Retuerto, M.; Croft, M.; Ignatov, A.; Fernández-Díaz, M. T. Crystal and magnetic structure of Sr_2MIR_6 ($\text{M} = \text{Ca}, \text{Mg}$) double perovskites: a neutron diffraction study. *Eur. J. Inorg. Chem.* **2013**, 178–185.
- (51) Kayser, P.; Alonso, J. A.; Mompeán, F. J.; Retuerto, M.; Croft, M.; Ignatov, A.; Fernández-Díaz, M. T. Crystal and magnetic structure of Sr_2MIR_6 ($\text{M} = \text{Sc}, \text{Ti}, \text{Fe}, \text{Co}, \text{In}$) in the framework of multivalent iridium double perovskites. *Eur. J. Inorg. Chem.* **2015**, 5027–5038.
- (52) Brese, N. E.; O'Keeffe, M. Bond-valence parameters for Solids. *Acta Crystallogr.* **1991**, *47*, 192–197.
- (53) Brown, I. D.; Altermatt, D. Bond-valence parameters obtained from a systematic analysis of the inorganic crystal structure database. *Acta Crystallogr.* **1985**, *41*, 244–247.
- (54) Macquart, R.; Kim, S.-J.; Gemmill, W. R.; Stalick, J. K.; Lee, Y.; Vogt, T.; zur Loye, H.-C. Synthesis, structure, and magnetic properties of $\text{Sr}_2\text{NiOsO}_6$ and $\text{Ca}_2\text{NiOsO}_6$: two new osmium-containing double perovskites. *Inorg. Chem.* **2004**, *44*, 9676–9683.
- (55) Ogale, A. S.; Ogale, S. B.; Ramesh, R.; Venkatesan, T. Octahedral cation site disorder effects on magnetization in double-perovskite $\text{Sr}_2\text{FeMoO}_6$: Monte Carlo simulation study. *Appl. Phys. Lett.* **1999**, *75*, 537–539.
- (56) Balcells, L.; Navarro, J.; Bibes, M.; Roig, A.; Martínez, B.; Fontcuberta, J. Cationic ordering control of magnetization in $\text{Sr}_2\text{FeMoO}_6$ double perovskite. *Appl. Phys. Lett.* **2001**, *78*, 781–783.
- (57) Serrate, D.; De Teresa, J. M.; Ibarra, M. R. Double perovskites with ferromagnetism above room temperature. *J. Phys.: Condens. Matter* **2006**, *19*, 023201.
- (58) Sánchez, D.; Alonso, J. A.; García-Hernández, M.; Martínez-Lope, M. J.; Martínez, J. L.; Mellergård, A. Origin of neutron magnetic scattering in antisite-disordered $\text{Sr}_2\text{FeMoO}_6$ double perovskites. *Phys. Rev. B: Condens. Matter Mater. Phys.* **2002**, *65*, 104426.
- (59) Narayanan, N.; Mikhailova, D.; Senyshyn, A.; Trots, D. M.; Laskowski, R.; Blaha, P.; Schwarz, K.; Fuess, H.; Ehrenberg, H. Temperature and composition dependence of crystal structures and magnetic and electronic properties of the double perovskites $\text{La}_{2-x}\text{Sr}_x\text{CoIrO}_6$ ($0 \leq x \leq 2$). *Phys. Rev. B: Condens. Matter Mater. Phys.* **2010**, *82*, 024403.
- (60) Wang, J.; Li, K.; Yu, B.; Wu, Z. Theoretical investigation on the magnetic and electronic properties of $\text{La}_2\text{NiIrO}_6$. *Comput. Mater. Sci.* **2012**, *60*, 149–152.
- (61) Kolchinskaya, A.; Komissinskiy, P.; Yazdi, M. B.; Vafaei, M.; Mikhailova, D.; Narayanan, N.; Ehrenberg, H.; Wilhelm, F.; Rogalev, A.; Alff, L. Magnetism and spin-orbit coupling in Ir-based double perovskites $\text{La}_{2-x}\text{Sr}_x\text{CoIrO}_6$. *Phys. Rev. B: Condens. Matter Mater. Phys.* **2012**, *85*, 224422.
- (62) Morrow, R.; Samanta, K.; Dasgupta, T. S.; Xiong, J.; Freeland, J. W.; Haskel, D.; Woodward, P. M. Magnetism in $\text{Ca}_2\text{CoOsO}_6$ and $\text{Ca}_2\text{NiOsO}_6$: unraveling the mystery of superexchange interactions between 3d and 5d ions. *Chem. Mater.* **2016**, *28*, 3666–3675.
- (63) Feng, H. L.; Reehuis, M.; Adler, P.; Hu, Z.; Nicklas, M.; Hoser, A.; Weng, S.-C.; Felser, C.; Jansen, M. Canted ferrimagnetism and giant coercivity in the non-stoichiometric double perovskite $\text{La}_2\text{Ni}_{1.19}\text{Os}_{0.81}\text{O}_6$. *Phys. Rev. B: Condens. Matter Mater. Phys.* **2018**, *97*, 184407.
- (64) Wu, W.; Kiryukhin, V.; Noh, H.-J.; Ko, K.-T.; Park, J.-H.; Ratcliff, W.; Sharma, P. A.; Harrison, N.; Choi, Y. J.; Horibe, Y.; Lee, S.; Park, S.; Yi, H. T.; Zhang, C. L.; Cheong, S.-W. Formation of pancakelike Ising domains and giant magnetic coercivity in ferrimagnetic LuFe_2O_4 . *Phys. Rev. Lett.* **2008**, *101*, 137203.
- (65) Yamamoto, A.; Hashizume, D.; Katori, H. A.; Sasaki, T.; Ohmichi, E.; Nishizaki, T.; Kobayashi, N.; Takagi, H. Ten layered hexagonal perovskite $\text{Sr}_5\text{Ru}_{5-x}\text{O}_{15}$ ($x = 0.90$), a weak ferromagnet with a giant coercive field $H_C \sim 12$ T. *Chem. Mater.* **2010**, *22*, 5712–5717.